Multitouch Pressure Sensing With Soft Optical Time-of-Flight Sensors

Ji-Tzuoh Lin, Christopher A. Newquist, and Cindy K. Harnett

***Abstract*— This article reports on optical time-of-flight (ToF) as a detection mode for soft optical deformation sensors. In this work, low-cost miniature light detection and ranging (LiDAR) chips recently developed for consumer mobile device applications perform real-time optical reflectometry at cm scales in soft optical waveguide networks. Our methods complement existing work by capturing spatial information that is lost with amplitude-only measurements. We demonstrate its application in a multitouch button system capable of extracting displacement values from soft optical switches with average error in the range of 100–200 microns on 1.75 mm of the switch travel. Because making reliable electronic connections to soft materials is a challenging task, we focus on minimizing connector count. In a tracking application, we find the centroid of an object on a three-point supported plate using three optical pressure switches connected to a single LiDAR sensor.**

***Index Terms*— Multiplexing, optical time-domain reflectometry, optical waveguides, pressure measurement, tactile sensors.**

I. Introduction

SOFT and flexible surfaces with a human-like sense of touch will lead to spatially aware robotic limbs, wearable devices capable of measuring subtle health changes, and medical prostheses that provide feedback to the user [1]–[3]. These applications motivate researchers to investigate ever softer and stretchier touch-sensitive materials [4]–[8].

Our own everyday sense of touch creates high expectations for force sensitivity, response speed, spatial resolution, and multitouch recognition in pressure-mapping sensors. Such features typically come at the cost of a high electronic connection count [9]. The instrumentation and measurement community has addressed the sensor density problem on two fronts: 1) by inventing new pressure transduction modes that pack spatial and amplitude information into a single sensing channel, including piezoelectric time-domain reflectometry in films [10] and cables [11] and 2) by improving multiplexing and data interpretation methods to extract higher spatial resolution from sparser arrays of sensors. Those approaches include electrical impedance tomography in low-density edge-fed impedance sensor arrays [12], and data analysis methods that embed knowledge about the spatial arrangement of the sensors [13].

Manuscript received August 25, 2021; revised December 9, 2021; accepted December 18, 2021. Date of publication January 7, 2022; date of current version February 24, 2022. The work of Ji-Tzuoh Lin and Christopher A. Newquist was supported by the U.S. National Science Foundation (NSF) under Award 1849213. The work of Cindy K. Harnett was supported by the NSF under Award 1935324. The Associate Editor coordinating the review process was Dr. Jae-Ho Han. *(Corresponding author: Cindy Harnett.)*

Ji-Tzuoh Lin and Cindy K. Harnett are with the Department of Electrical and Computer Engineering, University of Louisville, Louisville, KY 40208 USA (e-mail: c0harn01@louisville.edu).

Christopher A. Newquist was with the Department of Electrical and Computer Engineering, University of Louisville, Louisville, KY 40208 USA. He is now with Edaptive Computing, Inc., Dayton, OH 45458 USA.

This article has supplementary downloadable material available at https://doi.org/10.1109/TIM.2022.3141159, provided by the authors.

Digital Object Identifier 10.1109/TIM.2022.3141159

A. Reducing Connector Count in Soft Systems

Toward the goal of reduced connector count, researchers in robotics and human-computer interaction have made progress in high-dimensional pressure- and deformation-mapping applications by applying machine learning to multifrequency capacitive sensors [14], and to inter-fiber signals from an optical fiber bundle in translucent foam [15]. Another group simulated paths for liquid metal-filled stretch sensors, then pruned the paths that gave redundant information about the deformations they wanted to detect [16]. Still, others have investigated fiber-like sensing materials with internal structures as alternatives to edge-driven matrix-style sensor grids for signal localization: optoelectronic printable filaments that report the location of a laser on a 3-D printed surface [17], conductive fibers braided to create multiple intersections for capacitive radial position detection [18] as user input devices [19], and soft electronic fibers with resistive contact location and multiple force ranges for a pressure mapping application [20].

For soft materials, the connector problem is acute. Soft connector technology lags far behind that for conventional rigid circuit boards and glass touchscreens, largely because the hard-to-soft materials junction is prone to stress concentration and connector failure. Even with a mature connector technology, increasing the sensor density creates a data management problem independent of the materials system. Biological nervous systems are a daunting inspiration; mammalian bodies contain thousands of sensory receptors in a single limb alone [21]. However, they also offer some guidance: long-distance communication from the sensor to the cortex is made robust by encoding signals in the timing and frequency of neural spikes [22], [23] and doing processing near the sensor reduces communication complexity [24]. Methods that combine spatial and pressure data into a few channels to reduce both the connection count and the central processing requirements will help expand the capabilities of these emerging soft materials systems.

B. Time-of-Flight (ToF) Methods

Timing the reflection of an optical, acoustic, or electronic pulse is a measurement modality that combines spatial information (the flight time) with amplitude information (the intensity of the returning pulse). The single-point nature of ToF methods has already led to low connector count deformation mapping in some soft, flexible, and stretchable

TABLE I
POLYMER OPTICAL WAVEGUIDE STRAIN MAPPING METHODS

Waveguide material	Transduction mechanism	Spatial category	Measurement scheme	Source/detector size	Reference
Thermoplastic urethane fiber	Light loss at deformation site	Multipoint	Optical time domain analysis	Chip scale source and detector	(This paper)
Cast urethane waveguide	Light injection at deformation site	Quasi-distributed	Wavelength analysis	Chip scale detector, distributed LED source with integrated color filters	[37]
Perfluoro graded index plastic optical fiber	Brillouin scattering	Distributed	Brillouin optical correlation domain reflectometry	Optical benchtop	[38]
Perfluoro graded index POF	Rayleigh scattering	Distributed	Swept-wave interferometry	Optical benchtop	[39]
Polycarbonate, CYTOP POFs	Fiber Bragg grating (FBG)	Multipoint	Wavelength analysis	Spectrometer (Laptop-scale modules available)	[40] (polycarbonate), [41] (CYTOP)

domains. Acoustic ToF methods developed for waveguide length measurement [25] were adapted to soft tubes for human-computer interaction devices [26], and acoustic ToF data was analyzed by machine learning methods to detect the configurations of hollow soft robotic fingers [27]. In the electronic signal realm, single-point time-domain reflectometry has been applied to wires on stretchable surfaces to capture information about strain [28]. In this article, we use light distance and ranging (LiDAR) chips designed for mobile devices to extract spatial and pressure information from all-polymer soft optical waveguide networks undergoing mechanical deformation. Because the focus of this article is on low connector count, experiments use a single LiDAR sensor consisting of one emitter/receiver pair [Fig. 1(a)] connected to a soft optical waveguide or network.

The instrumentation and measurement community has contributed to the calibration, precision, and reliability of LiDAR systems using both modeling and hardware approaches [29]–[33]. The majority of LiDAR applications are in free space object detection and ranging, but in this article, the LiDAR signal travels through a solid, optically transmissive soft fiber. Optical fiber sensing methods, whether in conventional glass fibers or in softer materials, offer fast response speed, wavelength multiplexing using passive filters, and performance modification with dopants such as fluorophores and resonant nanoparticles.

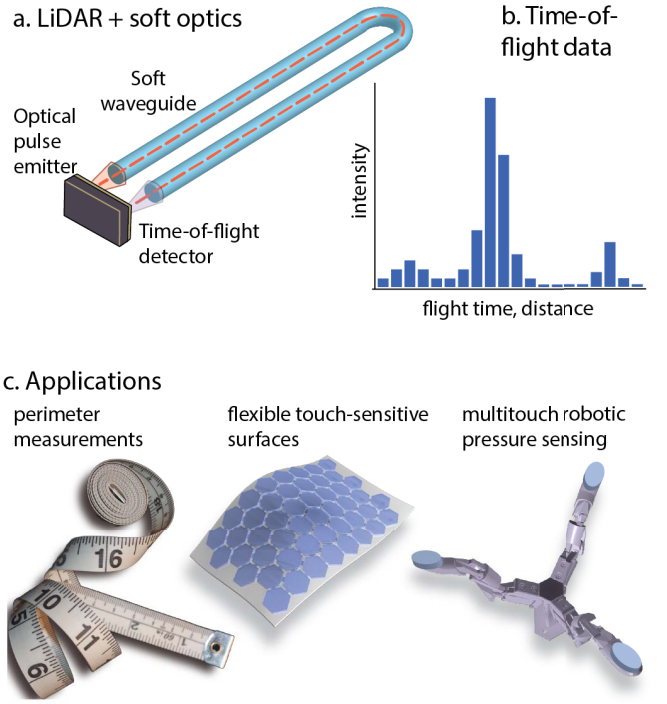

Fig. 1. (a) Miniature LiDAR sensors measure flight times in cm-scale soft optical waveguides. (b) Multitarget histogram data. (c) Applications for soft sensors that combine spatial and pressure data.

C. Optical Waveguide and Fiber-Based Methods

Unlike free-space camera or laser scanning methods for shape capture, optical fiber methods can perform high-speed measurements in embedded formats and in hidden structures, including locations obscured by opaque liquids, smoke, and fog. Toward pressure mapping, fiber Bragg grating (FBG) methods induce sensitivity to small changes in refractive index for chemical [34], pressure [35], and shape detection [36] while encoding spatial information in the reflected wavelength. While FBG fibers are not yet made from elastomeric materials capable of extreme deformation, polymer FBGs are emerging. Table I summarizes these and other methods for mapping mechanical strains with polymer optical waveguides, including polymer optical fibers (POFs).

Pressure mapping methods in extreme deformation environments have long been dominated by electronic sensors. Soft optical sensors have two key advantages versus soft electronic sensors made from conductive elastomeric composites: lower temperature sensitivity, and immunity to electromagnetic interference. The materials are deformable and often intrinsically stretchable, with similar mechanical properties to wearable

TABLE II
CHARACTERISTICS OF THERMOPLASTIC URETHANE FIBER MATERIAL IN THIS WORK

Numerical aperture	Diameter (mm)	Refractive index (visible)	Wavelength dispersion (ps/km per nm)	Extinction coefficient (dB/cm)	Tensile modulus (MPa)	% tensile elongation before break	Shore hardness
1.18	1.75	1.55	34 (typical) [57]	0.097	7.8	508	95A

stretch fabrics and soft robotic systems. Other advantages include the ability to send and receive signals across an air gap (common to capacitive sensors but not resistive ones), operation at infrared wavelengths that pass through tissue for biocompatible [42] and implantable [43] applications, and all-polymer construction that will not corrode when exposed to water. When the material is soft, mechanically induced color changes can even provide passive user feedback [44].

For these reasons, soft optical sensors are an increasingly active research area. In our earlier previous work on soft optical sensors [45], [46] and in that of others [3], [42], [43], [47]–[52]the transmitted light intensity is measured with a photodiode or other amplitude-based optoelectronic sensor on one end of the waveguide. The light source on the opposite end, or in a side-coupled LED or waveguide for encoding spatial data by time or wavelength multiplexing [37], [50], [53] is typically a light-emitting diode controlled by a digital output. While amplitude measurements are lightweight and straightforward, they have the drawback (in common with resistive sensors) that the transmitted signal is an integrated measurement. It combines stretching losses caused by increased absorption and scattering over a lengthened optical path, bending losses, and pressure-induced losses where wall deformations cause light to escape from the waveguide. Some of the spatial information in the amplitude signal is lost. Recently our group applied LiDAR sensors to stretchable optical fiber sensors [54], decoupling bending from stretching by using ToF to determine the length of the stretched fiber to within 1% independent of signal amplitude, but not yet investigating the spatial origin of the signal.

D. Multitouch Pressure Sensing With ToF in a Soft, Branched Optical Network

In this work, we apply the optical ToF approach to spatial mapping and, thanks to a low-cost consumer LiDAR sensor that reports a histogram of amplitude-versus-time [Fig. 1(b)], demonstrate combined pressure and location sensing with multitouch capability. Since most LiDAR chips report signal amplitude as well as flight time, the amplitude-based soft optical sensor systems recently reviewed in [55] and [56] will work with them, adding a new ToF data channel and, with many chips, an ambient-light data channel that can measure light originating from other sources than the ToF pulse. The novelty and contribution of this work are the simplicity of the source and detector compared to other methods in Table I, and construction from soft polymeric materials.

Our work in the rest of the article consists of experiments with ToF optical measurements in a multitouch button network. The following sections describe how ToF histograms were extracted from a commercial LiDAR chip, the design and characterization of pressure switches made from soft optical materials, and data analysis methods. The switch network is then demonstrated in a modular soft optical system capable of tracking an object's centroid based on its weight distribution on a multisensor plate using only three contact points and a single optoelectronic sensor.

II. METHODS

A. Sensor Chip and Interfacing Method

The LiDAR chip used in this work is a multitarget distance sensor (VL53L3CX, ST Microelectronics, Inc). This 2.4 × 4.4-mm module launches an optical pulse from its 940-nm laser, detects the returning light with an avalanche photodiode, and produces a histogram of ToF data [Fig. 1(b)]. A Nucleo microcontroller board (P-NUCLEO-53L3A2, ST Microelectronics, Inc.) drives the LiDAR chip and sends multitarget ranging results to a computer using a graphical user interface (GUI) to display object distances and signal intensities. Raw histogram data is not available in the GUI, but is available from the Nucleo through its low-level serial interface. Each bin in the ToF histogram corresponds to approximately 20-cm travel in air; 24 bins give it a range of 1 cm–5 m. During a ranging event, statistics are collected from several thousand pulses, and centroids are calculated for histogram features from large numbers of pulse power detection events, allowing for better than 20-cm resolution. The manufacturer's stated time/distance resolution is 6.6 ps (1 mm) and ranging accuracy is 3% depending on ambient light and target reflectance.

B. Design and Characterization of Soft Optical Pressure Switch Networks

A commercially available clear, 1.75-mm diameter thermoplastic polyurethane (TPU) 3-D printing filament was used as a soft waveguide to bring signals from the LiDAR chip to the switch network. This material (Clear BUILD series TPU, Matter Hackers, Inc., Lake Forest, CA, USA) has a Shore hardness of 95 A, making it highly flexible. Its index of refraction was 1.55 ± 0.02 in the visible, determined by immersion in index-matching liquids. We measured the fiber's attenuation at 0.097 dB/cm with a 940-nm LED source via the cutback test (Fig. S1). This waveguide is transmissive enough for the LiDAR chip to detect pulses through roundtrip path lengths of up to 1.8 m. Table II summarizes the specifications of this material. For this diameter of fiber at 940 nm, the fiber

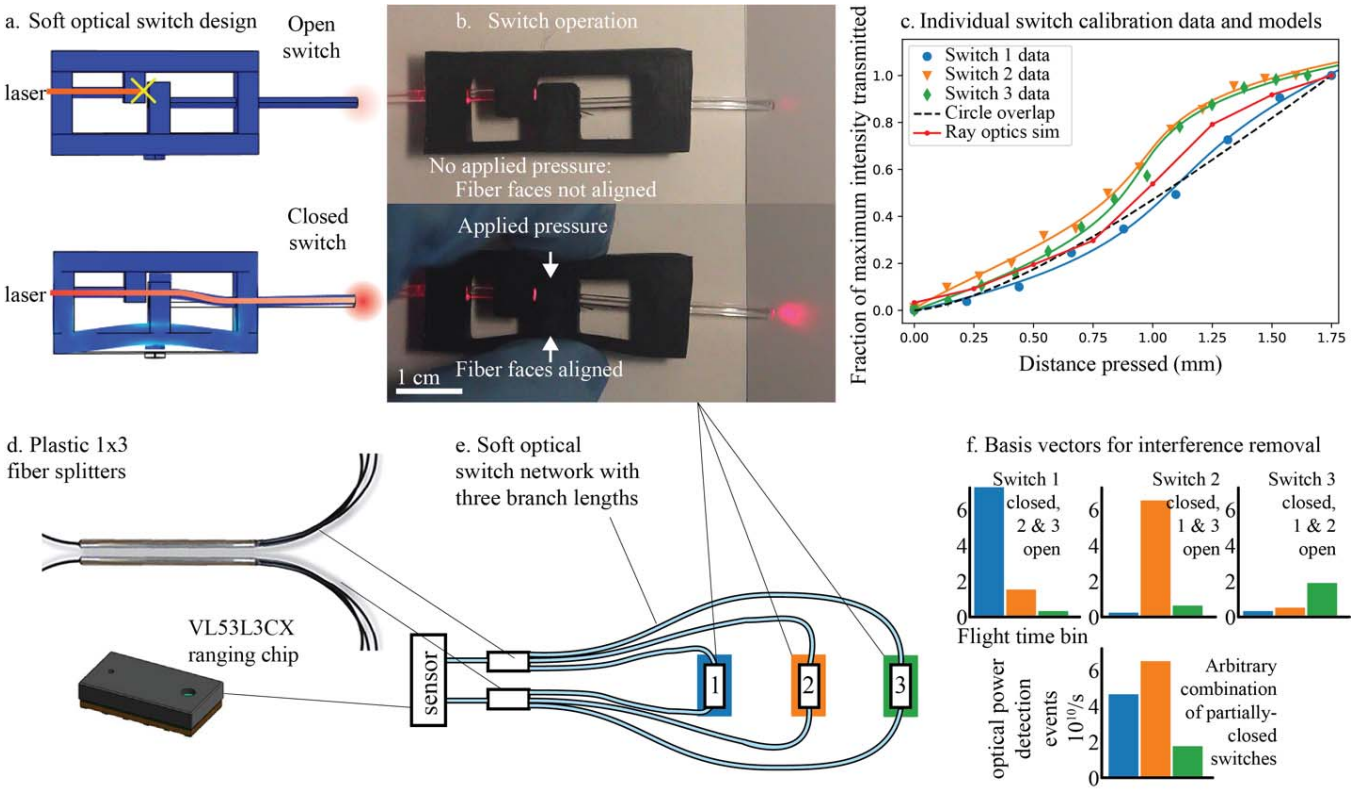

Fig. 2. (a) Soft optical pressure switch illustration and (b) photograph with laser. (c) Calibration curves for three switches. (d) and (e) Branched optical switch network components and layout. (f) Optical power in the three key histogram bins for each fully closed switch in the network.

is strongly multimode with approximately 2×10^6 guided modes [45]. While multimode fibers are subject to modal noise, the large diameter of these plastic optical fibers ensures that even if the fiber and source are slightly misaligned, most of the light is still launched along the center core, reducing modal noise [58].

All-polymer pressure-sensitive optical fiber switches were created from soft 3-D printed black TPU "normally open" fiber holders [Fig. 2(a) and (b)] that align two cut, 1.75-mm diameter TPU fiber faces when fully pressed (both black and clear filaments were Matter Hackers BUILD series TPU).

The dependence of transmitted intensity versus switch displacement is plotted for three switches in Fig. 2(c), along with a "circle overlap" model based on the fractional overlap area of two 1.75-mm diameter circles as the center-to-center distance varies from 1.75 mm (one full fiber diameter) to 0 (perfectly aligned). The moving circles represent the two fiber faces as the switch translates from open to closed. While this simple 2-D geometric model captures the general shape of the switch responses, a 3-D ray optics simulation (COMSOL Ray Optics) with 1 mm end-to-end separation more closely represents the steep slope of the curve at the center of the displacement range seen in two of the switches.

Variations in end-to-end separation during assembly and other manufacturing differences can create different intensity-versus-distance profiles within a batch of switches. To get displacements from optical intensity, we fit a 4th-degree polynomial to the individual switch calibration data in Fig. 2(c) and inverted it to calculate the displacement for a given switch based on its measured intensity signal.

Switch networks were created using plastic optical fiber 1-to-3 splitters [Fig. 2(d)] and couplers (Industrial Fiberoptics POF Coupler 1×3 IF 543 and IF CS4, respectively). Three switches were placed on paths of three different lengths [Fig. 2(e)] intended to create three distinct features in the ToF histogram. Total path lengths were 115, 146, and 167 cm. The two ends of the network were connected to the LiDAR sensor using a 3-D printed black plastic housing.

C. Testing Methods

1) Individual Switch Testing: Force versus displacement was characterized for individual switches by pressing them with a force probe (DFS20, NexTech, Inc.) and collecting intensity readings using a power meter (PM-100D, ThorLabs, Inc.) and 940-nm infrared LED source.

2) Multitouch Button Network Testing: For characterizing the multitouch button network, we used the Nucleo's low-level serial interface with Python code that accesses the serial port, to get access to unprocessed ToF histogram data from the VL53L3CX multitarget sensor. The network in Fig. 2(e) had "targets" at fixed locations with varying "reflectivity" controlled by switch closure, while the Nucleo's factory-designed ranging algorithms are meant to find peaks from targets at unknown locations. In this experiment, spatial information was captured in the sense of a lookup table, where 24 different flight time bins, each corresponding to a ~20-cm

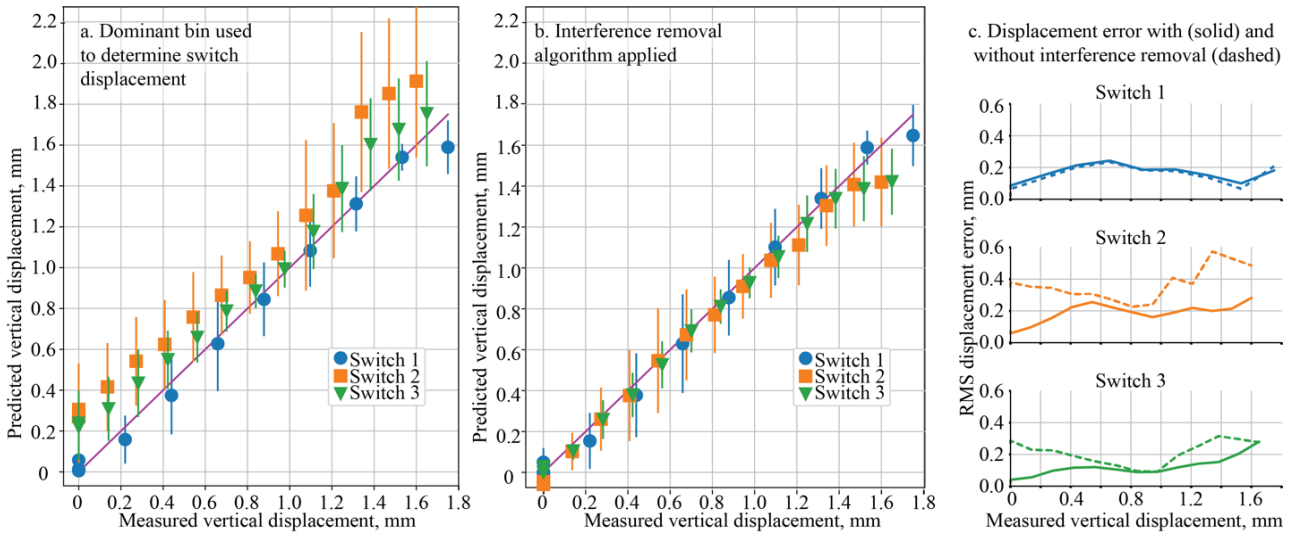

Fig. 3. (a) Switch displacements predicted from dominant bin value; (b) displacements with interference removed; and (c) error analysis.

light travel distance in air, are assigned to signals traveling specific distances from emitter to sensor. Plotting the raw histogram data allowed us to identify the key histogram bin associated with each switch.

To test the multitouch pressure measurement capabilities of the button network, we used three independent servomotors (Fig. S2) to depress the soft optical switches of Fig. 2 over a range of 10–12 displacements between 0 and 1.75 mm [the full diameter of the optical channel in Fig. 2(a)]. The Python program captured histogram data and showed real-time results picked from three key histogram bins out of the 24 available bins. During testing, the three servos were simultaneously run to adjust each of the three switches to a new displacement value. The positions were held for 2 s, and intensity data were recorded from the three key bins, along with the known servo positions. Switches were adjusted in random combinations of vertical displacements, and a total of 3605 data points were recorded for evaluation.

3) Object Tracking Plate Fabrication and Testing: In an application-oriented demonstration of the triple sensor network, we placed the three pressure switches at 120° angles supporting a plate (Fig. S3). When an object was placed on the plate, the distribution of force on the three switches depended on the object's location on the plate. To interpret the three key histogram bin readings as object locations, the video was collected and analyzed to compute the centroid of the rolling object. The general setup for object tracking is demonstrated in supplementary movie M1.

D. Modeling and Data Analysis Methods

1) Interference Removal Method: In the triple sensor network, although each switch dominates one bin in the histogram, some signal gets into neighboring bins because the laser pulse has a finite width and undergoes dispersion as it moves through the network. Because of this interference, reading the unknown pressure values from the three buttons is not as simple as reading a single intensity value from a specific flight time bin. Basis vectors [Fig. 2(f)] were therefore collected for each switch by fully pressing the switch while leaving the other two switches closed. These vectors were then used to construct a matrix M to disentangle the pressure signal on each button from multipress data, with the intensity values in each chart in the top row of Fig. 2(f) forming consecutive rows of M. The three corrected intensity values I_c were then computed as

$$I_c = I_r M^{-1} \tag{1}$$

where I_r is the vector of received intensity values in the three key histogram bins. The corrected intensity result is scaled between 0 (not pressed) to 1 (maximally pressed). This value is used to index into the displacement-versus-intensity calibration curves in Fig. 2(c) and predict a corrected displacement value for each switch.

2) Object Tracking Analysis Method: Real-time object tracking was implemented by making a lookup table from training data where the object was placed on the tracking plate at known (x, y) locations. During a tracking run, the three key histogram intensities were used to find the best match in the training data, and the matching (x, y) value was reported as the object's centroid. To generate the training data, optical sensor readings and overhead video were recorded simultaneously using a Raspberry Pi computer. The Python computer vision library Open CV was used to extract centroid values for an object (an apple) on the random training events that were collected in a training file structured as a Python dictionary. Each entry consisted of the received power amplitudes in the three sensors' key histogram bins, along with the video centroid as a pixel coordinate pair.

In the tracking application, the location was predicted in real-time by dictionary lookup of the nearest match, defined as the (x,y) location having the least difference of the sum of absolute values on each of the three sensors' signals in the dictionary

$$\text{Index}\{x, y\} = \text{Index}\left\{\min\left[\sum_{1}^{3} abs(S_i - S_{iL})\right]\right\}. \tag{2}$$

Here, S_i is the reading of the ith key histogram bin, S_{iL} is the reference sensor reading in the dictionary, min denotes the least value of all the calculated absolute values, and the index points to the location at (x,y).

The plate had a radius of 9 cm, meaning that each of the 2000 random training points represented an average area of 0.127 cm or a circle of radius 2 mm. Therefore, the best-case resolution of this lookup table method is approximately 2 mm. The predicted location was plotted live along with the apple's image and centroid on the plate.

III. Experimental Results

A. Individual Switch Results

Force versus transmitted intensity results for the individual switches while in the network are shown in Fig. S4. The force required to fully align the fibers for maximum light transmission was 12 N, with a minimum detectable force of 1 N.

B. Multitouch Button Network Results

Multitouch displacement data predicted from intensity readings for more than 10 000 individual switch settings are presented in Fig. 3(a), coded by the dominant bin for switches 1–3 and plotted against the known displacement value for that switch. For each plotted data point, the other two switches are at random displacements. The plots in Fig. 3(a) and (b) show the average value of the predicted displacement, with standard deviation error bars. Fig. 3(b) applies the interference removal method of (1) to correct for received power put into the bin by other switches, for example, where Switch 1 adds counts to the bin for Switch 2 (Fig. 2(f), the center plot in the top row). This linear regression helps put Switch 2 and 3 closer to the perfect-fit line running diagonally across Fig. 3(b), compared to Fig. 3(a), where predicted positions for Switch 2 and 3 appear high above their known values, especially at the ends of the range.

More quantitatively, Fig. 3(c) shows that the interference removal algorithm improves root mean square (rms) displacement error over most of the range for all but Switch 1. Switch 1, on the shortest path, transmits the highest intensity signal and its bin has almost no input from the other buttons, so the interference removal algorithm does little to improve on the result obtained directly from the dominant bin. For all switches over all but the last 0.25 mm of the pressure range, the rms error of the corrected value is less than ∼15% of the full range (1.75 mm). This result also contains error from fluctuations in received power intensity and error from the vibration of the servo motors during tests, which will not be corrected by the interference removal algorithm.

C. Object Tracking Demonstration

Fig. 4 shows the results from correlating the video centroid of an object [an apple, Fig. 4(a)] with the signals from the three-switch pressure plate. In Fig. 4(b), the video and sensor-predicted centroids are plotted as white and cyan dots, respectively, as the apple is rolled around on the plate. The average

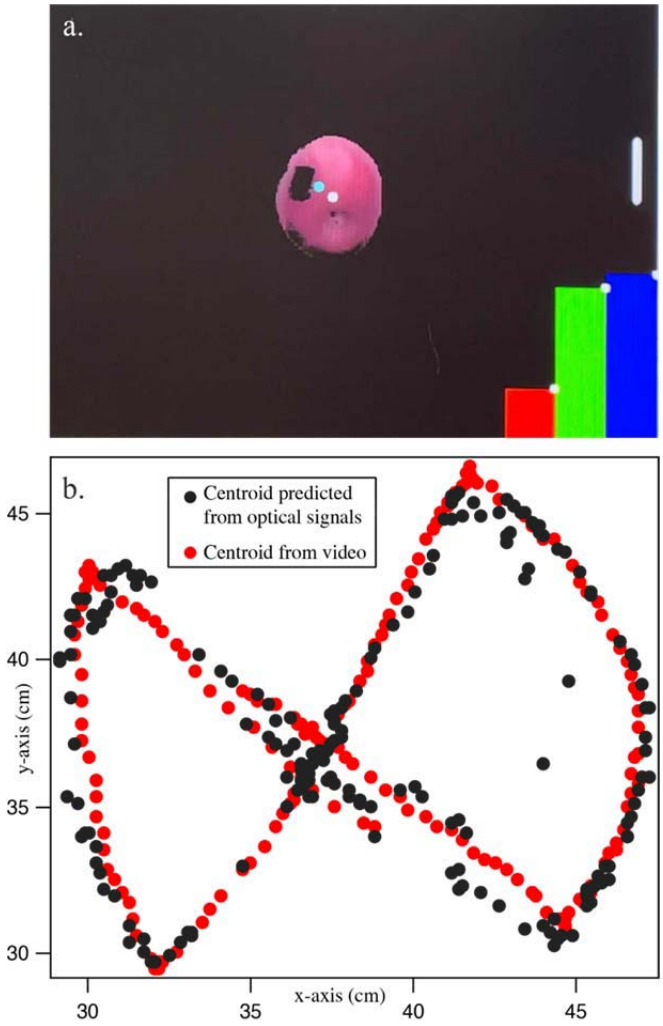

Fig. 4. Object tracking demonstration using the three-sensor network of Fig. 2(e) to support a pressure plate. (a) Video analysis of object centroid in real-time with optical sensor data at lower left. (b) Trajectory of object centroid predicted from optical sensor network compared with video.

distance difference between video and sensor-predicted centroids along the trajectory of Fig. 4 was 9.1 pixels. With a span of 160 pixels across the 18-cm diameter plate, the average tracking error was approximately 1 cm.

Sources of this tracking error include light overlapping the key histogram bin as discussed earlier, hysteresis in the switches' elastic properties, errors in the determination of the centroid locations introduced by the lighting conditions for the apple, and time latency between the moving images and the three switch signals.

We also observed that the optical switches worked in water (index of refraction ∼1.33), which has a lower refractive index than the TPU fiber core. The switch was pressed while submerged in a beaker, and real-time histograms showed a response similar to that in air.

IV. Conclusions and Future Work

In this article, we demonstrated multitarget optical ToF sensing of lengths and deformations in soft structures with

a single-point optical sensor. The all-polymer sensor elements offer promise for wearable, washable shape capture systems and touch-sensitive robotic skins, and the ability to perform in water illustrates a key advantage of optics versus electronics. Such systems may be a good match to underwater, damp, or messy environments, including robotic grip and balance sensors for handling materials in food, beverage, and medical applications.

Challenges remain in several areas: quickly and uniformly assembling connectors onto the ends of soft waveguides, increasing the optical transmission of soft materials, developing new soft optical materials that can control inter-fiber light transmission in response to pressure for force-sensitive touchpads, improving the sampling rate (currently 30 Hz) for high-speed applications, and improving the spatial resolution of ToF histogram data for finer-grained deformation mapping. Although a 30-Hz sampling rate means the system is limited to low-speed applications, the sensor is vibration tolerant because each measurement averages results from several thousand sub-microsecond laser pulse periods during the sampling period.

Currently, to obtain simultaneous displacement data for the three switches in the multitouch button network experiments, the fiber network lengths needed to be separated by at least 20 cm so two switches would not dominate the same histogram bin. Separations were made even longer than that to reduce interference from pulse broadening. Meter-scale fiber lengths may work for robotic limb sensors when coiled, but are undesirable for smaller-scale touchpads, grip sensors, and skins. Higher spatial resolution LiDAR sensors will help shrink the sensor size. Driven by augmented reality applications and by a market where LiDAR chips are already installed in billions of consumer devices, chipmakers continue increasing the bandwidth and resolution of their products while keeping chip size and power consumption small.

To return to a biological inspiration, doing some signal processing near the sensor helps minimize communication traffic and allows the cortex to be organized by function rather than by exact sensor location. For these soft optical sensors, the local processing could be electronic, but there are also possibilities for mechanical deformations to shift new branches into the network, changing the structure and meaning of the ToF data.

ACKNOWLEDGMENT

The authors would like to acknowledge Douglas Lin for writing Python code to do real-time data visualization, Paul Bupe, Jr. for graphical abstract editing, and John Rossi and John Kvam at ST Microelectronics for providing information on the VL53L3CX sensor.

REFERENCES

[1] H. Lim, H. S. Kim, R. Qazi, Y. Kwon, J. Jeong, and W. Yeo, "Advanced soft materials, sensor integrations, and applications of wearable flexible hybrid electronics in healthcare, energy, and environment," *Adv. Mater.*, vol. 32, no. 15, Apr. 2020, Art. no. 1901924.

[2] M. M. Iskarous and N. V. Thakor, "E-skins: Biomimetic sensing and encoding for upper limb prostheses," *Proc. IEEE*, vol. 107, no. 10, pp. 2052–2064, Oct. 2019.

[3] H. Zhao, K. O'Brien, S. Li, and R. F. Shepherd, "Optoelectronically innervated soft prosthetic hand via stretchable optical waveguides," *Sci. Robot.*, vol. 1, no. 1, Dec. 2016, Art. no. eaai7529.

[4] S. Y. Kim *et al.*, "Sustainable manufacturing of sensors onto soft systems using self-coagulating conductive Pickering emulsions," *Sci. Robot.*, vol. 5, no. 39, Feb. 2020, Art. no. eaay3604.

[5] S. Han *et al.*, "Battery-free, wireless sensors for full-body pressure and temperature mapping," *Sci. Transl. Med.*, vol. 10, no. 435, pp. 1–14, Apr. 2018.

[6] J. T. Muth *et al.*, "Embedded 3D printing of strain sensors within highly stretchable elastomers," *Adv. Mater.*, vol. 26, no. 36, pp. 6307–6312, 2014.

[7] A. Atalay *et al.*, "Batch fabrication of customizable silicone-textile composite capacitive strain sensors for human motion tracking," *Adv. Mater. Technol.*, vol. 2, no. 9, Sep. 2017, Art. no. 1700136.

[8] F. Shahmiri and P. H. Dietz, "ShArc: A geometric technique for multi-bend/shape sensing," in *Proc. CHI Conf. Hum. Factors Comput. Syst.*, Honolulu, HI, USA, Apr. 2020, pp. 1–12.

[9] B. Shih *et al.*, "Electronic skins and machine learning for intelligent soft robots," *Sci. Robot.*, vol. 5, no. 41, pp. 1–12, Apr. 2020.

[10] A. Kimoto and S. Shimada, "A proposal of new multifunctional pressure sensor based on PVDF films," *IEEE Trans. Instrum. Meas.*, vol. 62, no. 10, pp. 2870–2877, Oct. 2013.

[11] A. Scheuermann and C. Huebner, "On the feasibility of pressure profile measurements with time-domain reflectometry," *IEEE Trans. Instrum. Meas.*, vol. 58, no. 2, pp. 467–474, Feb. 2009.

[12] Y. J. Jeong, Y. E. Kim, K. J. Kim, E. J. Woo, and T. I. Oh, "Multilayered fabric pressure sensor for real-time piezo-impedance imaging of pressure distribution," *IEEE Trans. Instrum. Meas.*, vol. 69, no. 2, pp. 565–572, Feb. 2020.

[13] H. Liu, D. Guo, and F. Sun, "Object recognition using tactile measurements: Kernel sparse coding methods," *IEEE Trans. Instrum. Meas.*, vol. 65, no. 3, pp. 656–665, Mar. 2016.

[14] H. A. Sonar, M. C. Yuen, R. Kramer-Bottiglio, and J. Paik, "An any-resolution pressure localization scheme using a soft capacitive sensor skin," in *Proc. IEEE Int. Conf. Soft Robot. (RoboSoft)*, Apr. 2018, pp. 170–175.

[15] I. M. Van Meerbeek, C. M. De Sa, and R. F. Shepherd, "Soft optoelectronic sensory foams with proprioception," *Sci. Robot.*, vol. 3, no. 24, pp. 1–8, Nov. 2018.

[16] J. Tapia, E. Knoop, M. Mutný, M. A. Otaduy, and M. Bächer, "MakeSense: Automated sensor design for proprioceptive soft robots," *Soft Robot.*, vol. 7, no. 3, pp. 332–345, Jun. 2020.

[17] G. Loke *et al.*, "Structured multimaterial filaments for 3D printing of optoelectronics," *Nature Commun.*, vol. 10, no. 1, p. 4010, Sep. 2019.

[18] A. Olwal, J. Moeller, G. Priest-Dorman, T. Starner, and B. Carroll, "I/O Braid: scalable touch-sensitive lighted cords using spiraling, repeating sensing textiles and fiber optics," in *Proc. 31st Annu. ACM Symp. User Interface Softw. Technol.*, Berlin, Germany, Oct. 2018, pp. 485–497.

[19] A. Olwal, T. Starner, and G. Mainini, "E-textile microinteractions: Augmenting twist with flick, slide and grasp gestures for soft electronics," in *Proc. CHI Conf. Hum. Factors Comput. Syst.*, Honolulu, HI, USA, Apr. 2020, pp. 1–13.

[20] A. Leber *et al.*, "Compressible and electrically conducting fibers for large-area sensing of pressures," *Adv. Funct. Mater.*, vol. 30, no. 1, Jan. 2020, Art. no. 1904274.

[21] A. Prochazka, "Sensory control of normal movement and of movement aided by neural prostheses," *J. Anatomy*, vol. 227, no. 2, pp. 167–177, Aug. 2015.

[22] F. McGlone and D. Reilly, "The cutaneous sensory system," *Neurosci. Biobehav. Rev.*, vol. 34, no. 2, pp. 148–159, Feb. 2010.

[23] M. Campero, J. Serra, H. Bostock, and J. L. Ochoa, "Slowly conducting afferents activated by innocuous low temperature in human skin," *J. Physiol.*, vol. 535, no. 3, pp. 855–865, Sep. 2001.

[24] B. C.-K. Tee *et al.*, "A skin-inspired organic digital mechanoreceptor," *Science*, vol. 350, no. 6258, pp. 313–316, Oct. 2015.

[25] D. Donlagic, M. Zavrsnik, and I. Sirotic, "The use of one-dimensional acoustical gas resonator for fluid level measurements," *IEEE Trans. Instrum. Meas.*, vol. 49, no. 5, pp. 1095–1100, Oct. 2000.

[26] C. E. Tejada, J. McIntosh, K. A. Bergen, S. Boring, D. Ashbrook, and A. Marzo, "EchoTube: Robust touch sensing along flexible tubes using waveguided ultrasound," in *Proc. ACM Int. Conf. Interact. Surf. Spaces*, Daejeon, South Korea, Nov. 2019, pp. 147–155.

[27] G. Zoller, V. Wall, and O. Brock, "Acoustic sensing for soft pneumatic actuators," in *Proc. IEEE/RSJ Int. Conf. Intell. Robots Syst. (IROS)*, Oct. 2018, pp. 6986–6991.

[28] R. Wimmer and P. Baudisch, "Modular and deformable touch-sensitive surfaces based on time domain reflectometry," in *Proc. 24th Annu. ACM Symp. User Interface Softw. Technol. (UIST)*, Santa Barbara, CA, USA, 2011, pp. 517–526.
[29] L. J. Koerner, "Models of direct time-of-flight sensor precision that enable optimal design and dynamic configuration," *IEEE Trans. Instrum. Meas.*, vol. 70, pp. 1–9, 2021.
[30] Z. Hu, Y. Li, N. Li, and B. Zhao, "Extrinsic calibration of 2-D laser rangefinder and camera from single shot based on minimal solution," *IEEE Trans. Instrum. Meas.*, vol. 65, no. 4, pp. 915–929, Feb. 2016.
[31] J. Holma, I. Nissinen, J. Nissinen, and J. Kostamovaara, "Characterization of the timing homogeneity in a CMOS SPAD array designed for time-gated Raman spectroscopy," *IEEE Trans. Instrum. Meas.*, vol. 66, no. 7, pp. 1837–1844, Jul. 2017.
[32] D. Li, M. Liu, R. Ma, and Z. Zhu, "An 8-ch LIDAR receiver based on TDC with multi-interval detection and real-time *In Situ* calibration," *IEEE Trans. Instrum. Meas.*, vol. 69, no. 7, pp. 5081–5090, Jul. 2020.
[33] B. Fu, Y. Wang, X. Ding, Y. Jiao, L. Tang, and R. Xiong, "LiDAR-camera calibration under arbitrary configurations: Observability and methods," *IEEE Trans. Instrum. Meas.*, vol. 69, no. 6, pp. 3089–3102, Jun. 2020.
[34] X.-D. Wang and O. S. Wolfbeis, "Fiber-optic chemical sensors and biosensors (2013–2015)," *Anal. Chem.*, vol. 88, no. 1, pp. 203–227, Jan. 2016.
[35] P. Roriz, O. Frazão, A. B. Lobo-Ribeiro, J. L. Santos, and J. A. Simões, "Review of fiber-optic pressure sensors for biomedical and biomechanical applications," *J. Biomed. Opt.*, vol. 18, no. 5, p. 50903, 2013.
[36] M. Jang, J. S. Kim, S. H. Um, S. Yang, and J. Kim, "Ultra-high curvature sensors for multi-bend structures using fiber Bragg gratings," *Opt. Exp.*, vol. 27, no. 3, pp. 2074–2084. Feb. 2019.
[37] H. Bai, S. Li, J. Barreiros, Y. Tu, C. R. Pollock, and R. F. Shepherd, "Stretchable distributed fiber-optic sensors," *Science*, vol. 370, no. 6518, pp. 848–852, Nov. 2020.
[38] N. Hayashi, Y. Mizuno, and K. Nakamura, "Distributed Brillouin sensing with centimeter-order spatial resolution in polymer optical fibers," *J. Lightw. Technol.*, vol. 32, no. 21, pp. 3999–4003, Nov. 1, 2014.
[39] S. T. Kreger, A. K. Sang, D. K. Gifford, and M. E. Froggatt, "Distributed strain and temperature sensing in plastic optical fiber using Rayleigh scatter," *Proc. SPIE*, vol. 7316, May 2009, pp. 85–92.
[40] A. Fasano *et al.*, "Fabrication and characterization of polycarbonate microstructured polymer optical fibers for high-temperature-resistant fiber Bragg grating strain sensors," *Opt. Mater. Exp.*, vol. 6, no. 2, pp. 649–659, Feb. 2016.
[41] R. Ishikawa *et al.*, "Strain dependence of perfluorinated polymer optical fiber Bragg grating measured at different wavelengths," *Jpn. J. Appl. Phys.*, vol. 57, no. 3, Feb. 2018, Art. no. 038002.
[42] J. Guo *et al.*, "Highly stretchable, strain sensing hydrogel optical fibers," *Adv. Mater.*, vol. 28, no. 46, pp. 10244–10249, Dec. 2016.
[43] J. Feng, Y. Zheng, S. Bhusari, M. Villiou, S. Pearson, and A. Campo, "Printed degradable optical waveguides for guiding light into tissue," *Adv. Funct. Mater.*, vol. 30, no. 45, Sep. 2020, Art. no. 2004327.
[44] J. D. Sandt *et al.*, "Stretchable optomechanical fiber sensors for pressure determination in compressive medical textiles," *Adv. Healthcare Mater.*, vol. 7, no. 15, Aug. 2018, Art. no. 1800293.
[45] C. K. Harnett, H. Zhao, and R. F. Shepherd, "Stretchable optical fibers: Threads for strain-sensitive textiles," *Adv. Mater. Technol.*, vol. 2, no. 9, Sep. 2017, Art. no. 1700087.
[46] S. Ceron, I. Cohen, R. Shepherd, J. Pikul, and C. Harnett, "Fiber embroidery of self-sensing soft actuators," *Biomimetics*, vol. 3, no. 3, p. 24, Sep. 2018.
[47] A. Leber, B. Cholst, J. Sandt, N. Vogel, and M. Kolle, "Stretchable thermoplastic elastomer optical fibers for sensing of extreme deformations," *Adv. Funct. Mater.*, vol. 29, no. 5, Feb. 2019, Art. no. 1802629.
[48] Z. Cai, W. Qiu, G. Shao, and W. Wang, "A new fabrication method for all-PDMS waveguides," *Sens. Actuators A, Phys.*, vol. 204, pp. 44–47, Dec. 2013.
[49] E. N. Udofia and W. Zhou, "3D printed optics with a soft and stretchable optical material," *Additive Manuf.*, vol. 31, Jan. 2020, Art. no. 100912.
[50] A. Leal-Junior, L. Avellar, A. Frizera, and C. Marques, "Smart textiles for multimodal wearable sensing using highly stretchable multiplexed optical fiber system," *Sci. Rep.*, vol. 10, no. 1, p. 13867, Aug. 2020.
[51] C. K. Asawa and S.-K. Yao, "Microbending of optical fibers for remote force measurement," U.S. Patent 4 421 979, Dec. 20, 1983.
[52] A. Massaro, F. Spano, A. Lay-Ekuakille, P. Cazzato, R. Cingolani, and A. Athanassiou, "Design and characterization of a nanocomposite pressure sensor implemented in a tactile robotic system," *IEEE Trans. Instrum. Meas.*, vol. 60, no. 8, pp. 2967–2975, Aug. 2011.
[53] P. A. Xu, A. K. Mishra, H. Bai, C. A. Aubin, L. Zullo, and R. F. Shepherd, "Optical lace for synthetic afferent neural networks," *Sci. Robot.*, vol. 4, no. 34, Sep. 2019, Art. no. eaaw6304.
[54] J.-T. Lin and C. K. Harnett, "Absolute length sensor based on time of flight in stretchable optical fibers," *IEEE Sensors Lett.*, vol. 4, no. 10, pp. 1–4, Oct. 2020.
[55] J. Guo, C Yang, Q. Dai, and L. Kong, "Soft and stretchable polymeric optical waveguide-based sensors for wearable and biomedical applications," *Sensors*, vol. 19, no. 17, p. 3771, Aug. 2019.
[56] W. Peng and H. Wu, "Flexible and stretchable photonic sensors based on modulation of light transmission," *Adv. Opt. Mater.*, vol. 7, no. 12, Jun. 2019, Art. no. 1900329.
[57] J. Y. Jang and J. Y. Do, "Synthesis and evaluation of thermoplastic polyurethanes as thermo-optic waveguide materials," *Polym. J.*, vol. 46, no. 6, pp. 349–354, Mar. 2014.
[58] M. Matsuura, R. Furukawa, Y. Matsumoto, A. Inoue, and Y. Koike, "Evaluation of modal noise in graded-index silica and plastic optical fiber links for radio over multimode fiber systems," *Opt. Exp.*, vol. 22, no. 6, pp. 6562–6568, Mar. 2014.

Ji-Tzuoh Lin received the Ph.D. degree in electrical engineering from the University of Louisville, Louisville, KY, USA, in 2006.

He is currently a Research Engineer with the University of Louisville. His doctoral studies were to develop MEMS spinal fusion sensors and the respective telemetry system. After graduation, he extended his research interests to MEMS devices that enable small-scale vibrational energy harvesting and micro-explosion. In this period, he was specifically interested in low-power MEMS solutions for sensors and actuators. During the past few years, the focus turned to radiation detection with MEMS resonators for space application. He started a company and received the SBIR Award, has an issued patent, two book chapters, and 20 peer-reviewed journal publications. He is currently working on research involving optical time of flight (ToF) sensors and polymer strain gauges. Both areas will be used for robotic interfaces for strain, location, and environmental detection.

Christopher A. Newquist received the B.S. degree in electrical and computer engineering from the University of Louisville, Louisville, KY, USA, in 2020.

From 2020 to 2021, he worked as a Robotics Laboratory Research Assistant, conducting experiments in soft and conventional robotics, writing software in ROS and OpenCV, and performing finite element simulations. During engineering school, he worked with the Next Generation Systems Laboratory, University of Louisville, and AndyMark, Kokomo, IN, USA. He is currently a Developer with Edaptive Computing Inc, Dayton, OH, USA. Both efforts were in the areas of robotics, circuit board design, sensor evaluation, and fabrication. He participated in FIRST Robotics for three years in high school and became a FIRST Robotics Competition Mentor after graduation.

Cindy K. Harnett received the B.S. degree in physics from Harvey Mudd College, Claremont, CA, USA, in 1993, and the Ph.D. degree applied and engineering physics from Cornell University, Ithaca, NY, USA, in 2000.

She is currently a Professor in electrical and computer engineering with the University of Louisville, Louisville, KY, USA, working on robotic sensing and actuating materials and compliant structures. Her long-term research vision is a faster route to put newly developed materials to work in sensor and actuator applications. On the smaller end of the size scale, compliant microelectromechanical devices show promise for bringing sensing functions to soft materials. Her current research aims at solving this materials integration problem with automation.